Full-f gyrokinetic particle simulation of centrally heated global ITG turbulence from magnetic axis to edge pedestal top in a realistic tokamak geometry

S. Ku[1],[*] C.S. Chang[1,2],[†] and P.H. Diamond[3]

[1]*Courant Institute of Mathematical Sciences,*
New York University, NY 10012, USA
[2]*Department of Physics, Korea Advanced Institute of Science and Technology,*
Daejon, Republic of Korea 305-701 and
[3]*CASS and Department of Physics, University of California,*
San Diego, La Jolla, California 92093, USA[†]

(Dated: August 15, 2009)

Abstract

Global electrostatic ITG turbulence physics, together with background dynamics, has been simulated in realistic tokamak core geometry using XGC1, a full-function 5D gyrokinetic particle code. Adiabatic electron model has been used. Some verification exercises of XGC1 have been presented. The simulation volume extends from the magnetic axis to the pedestal top inside the magnetic separatrix. Central heating is applied, and a number, momentum, and energy conserving linearized Monte-Carlo Coulomb collision is used. In the turbulent region, the ion temperature gradient profile self-organizes globally around $R/L_T = (Rd\log T/dr = $ major radius on magnetic axis/temperature gradient length) $\simeq 6.5 - 7$, which is somewhat above the conventional nonlinear criticality of $\simeq 6$. The self-organized ion temperature gradient profile is approximately stiff against variation of heat source magnitude. Results indicate that the relaxation to a self-organized state proceeds in two phases,namely a transient phase of excessively bursty transport followed by a $1/f$ avalanching phase. The bursty behaviors are allowed by the quasi-periodic collapse of local E × B shearing barriers.

*Electronic address: `sku@cims.nyu.edu`

†Electronic address: `cschang@cims.nyu.edu`

I. INTRODUCTION

In a laboratory plasma without a large scale MHD instability, a turbulent plasma self-organizes to a global profile in which the heat source, the momentum source, the particle source, the turbulence phenomena, the neoclassical phenomena, and the background plasma profile are part of the global self-organization feed-back loop. Within this self-organizing loop, experimentalists can only control the sources and sinks (to a less degree) if the confinement geometry is given. The rest of the important observables develop as a result. In order to enhance the predictive simulation capability for tokamak plasma performance, including ITER [1], it is desirable to study turbulent and the neoclassical plasma dynamics self-consistently in a full-function (full-f) simulation code with proper sources and sinks. The resulting plasma behaviors (such as turbulence spectrum, transport, plasma profiles, etc) are to be compared with experimental observations. A few such codes are emerging in the international research community [2–4].

The ITG-driven (ion temperature gradient driven) modes, if driven unstable, are known to drive robust turbulence activity which may dominate tokamak transport phenomena [5, 6]. Moreover, ITG turbulence energy inverse-cascades to form large scale streamers, and also drives Reynolds stresses which influence mean and zonal toroidal and poloidal flows on scales far in excess of ion gyroradius ρ_i.

We report on global electrostatic ITG-driven simulation result from the full-f gyrokinetic particle code XGC1 [7, 8] in a realistic tokamak geometry, which also includes self-consistent mean dynamics of the plasma (excluding the evolution of the mean magnetic flux, current-density and q profile). Evolution of the mean plasma is driven by both neoclassical and turbulent effects. The present simulation volume extends from the magnetic axis to an edge pedestal top radius at $\psi_N = 0.9$ (where ψ_N is the poloidal magnetic flux ψ normalized to be 0 on the magnetic axis and 1 at the magnetic separatrix) over the whole toroidal angle. A strong heat source is placed around the magnetic axis. While the plasma ions are simulated with full-f marker particles, electron response is assumed to be adiabatic in the present study. Neoclassical solutions with full-f electrons and ions have been reported elsewhere [7]. Coulomb collisions are modeled by a well-known particle, momentum, and energy conserving linearized Monte-Carlo scheme[9–12], which uses delta-f concept by approximating the background field particles as Maxwellian and which has been shown to reproduce neoclassi-

cal physics in full-f mode [7, 13, 14]. In this scheme, the conservation property is assured by adjustment of the particle weights. In a full-f simulation, the particle weights are invariant during the time advance process (Vlasov part of the Fokker-Planck equation). However, the particle weights are allowed to change in the collision process. We note here that there are other full-f collision algorithms which demand the conservation by shifting and scaling of the particle velocities [15].

The work presented here is electrostatic and constitutes only a first step toward achieving a desirable predictive capability. A true predictive capability of a plasma discharge requires not only magnetic field fluctuations, but also evolution of the plasma current profile and magnetic equilibrium, MHD dynamics, and the interaction of the turbulence with the plasma current profile and MHD dynamics (which includes tearing modes, shear Alfven modes, kinetic ballooning modes, edge localized mode, resistive wall modes, etc).

The aim of this report is to elucidate the dynamics of turbulence and plasma relaxation to a quasi-stationary self-organized state [16, 17] with a heat source[18] in the full-f code XGC1. We identify two stage processes wherein: (a) The first stage is a bursty cycle, marked by development of bursty turbulent heat flux interconnected with collapses of the self-generated $E \times B$ shear. (b) The second stage is more akin to avalanching near a self-organized critical (SOC) state. In this state, the turbulent heat flux shows a 1/f type frequency spectrum, except for the geodesic acoustic mode activities at high frequency (with the bursty behavior reduced to obey the $1/f$ spectrum), and the ion temperature profile saturates globally around a roughly constant R/L_T values $\simeq 6.5 - 7$ ($\equiv R \, d \log T/dr = $ major radius/temperature gradient length), which is somewhat above the nonlinear stability boundary $R/L_T \simeq 6$ [19]. Settling down of the initial heat bursts into an avalanche state is similar to the recent observation made in Ref. [2]. The central heat source region shows different turbulence activity from the source-free region in that the subcritical strong turbulence, the strong $E \times B$ shearing and the strong transport exist without the bursty phenomenon.

A brief description of the full-f XGC1 gyrokinetic code and the several representative verification exercises are given in Sections II and III, respectively. The simulation results are presented in Sec. IV, followed by conclusion and discussion in Section V.

4

II. THE FULL-F GYROKINETIC CODE XGC1

XGC1 is a full-f gyrokinetic particle-in-cell code [7, 8] which can simulate the whole plasma volume including the magnetic axis, the magnetic separatrix and the biased material wall, by reading in a g-eqdsk data file generated from experimental equilibrium reconstruction [20]. XGC1 in its present form is an electrostatic code. Full-f marker ions and adiabatic electrons are used in the present study of ITG turbulence. A heat source is placed at the inner radial boundary to induce a heat flux into the simulation region, and a heat sink is sometimes placed at the outer boundary. Heat source (sink) is normally modeled by raising (lowering) the particle energy in the source (sink) region by a small fraction of particle kinetic energy while keeping the pitch angle invariant. A heat source is always necessary to maintain a radial heat flux, but a heat sink is not necessary in a short time simulation since the heat can be allowed to accumulate at the outer boundary, where temperature is the lowest, with a rise in the local temperature there. A particle, momentum and energy conserving linear Monte-Carlo Coulomb collision operator is built into the particle motion, as described in the previous section Ref. [9–13]. Monte Carlo neutral particles can also be simulated together in the full-f XGC family codes [13]. In the present short time simulation, however, the neutral particle routine is not used.

Marker particles follow the electrostatic Lagrangian equation of motion which conserves the mass, canonical angular momentum and energy [21–23].

$$
\begin{align}
\dot{\mathbf{X}} &= (1/D)[v_\parallel \hat{b} + (v_\parallel^2/B)\nabla B \times \hat{b} + \{\mathbf{B} \times (\mu \nabla B - \mathbf{E})\}/B^2] \tag{1} \\
\dot{v}_\parallel &= -(1/D)(\mathbf{B} + v_\parallel \nabla B \times \hat{b}) \cdot (\mu \nabla B - \mathbf{E}) \\
D &= 1 + (v_\parallel/B)\,\hat{b} \cdot (\nabla \times \hat{b}),
\end{align}
$$

where $v_\parallel$ is the speed of the particle parallel to the local magnetic field vector $\mathbf{B}$, $\hat{b} = \mathbf{B}/B$, $\mu = v_\perp^2/2B$ is the magnetic moment, and $\mathbf{E}$ is the gyro-averaged electric field. A particular feature in XGC1 is the use of a cylindrical coordinate system for the particle advance, which allows particle motion in a true arbitrary shaped flux surfaces including the magnetic separatrix and the magnetic X-point. In a conventional magnetic flux coordinate system, the equation of motion encounters a mathematical singularity on the magnetic separatrix surface and the error in the particle motion grows rapidly as it approaches the magnetic separatrix.

5

In order to take advantage of the slowly varying nature of the electric potential (both neoclassical and turbulent) along the magnetic field lines, the electrostatic potential is solved on an approximately field-line following mesh as is usually done in conventional turbulence codes. Meshes on all the poloidal plane are identical (axisymmetric). When a mesh node is mapped along the magnetic field line, it meets approximately another mesh node on the adjacent poloidal plane. The mapping is only approximate because the magnetic field lines do not close unless on mode rational surface. Due to the field-line following mesh in the existence of the magnetic X-point, large flux volume expansion along the field lines, and arbitrary wall shape, an unstructured triangular mesh system is used in the radial-poloidal plane (and regular in the toroidal direction) at the expense of computing time. The snapshot particle characteristics are mapped to the cell nodes for electric field calculation from the gyrokinetic Poisson equation (quasi-neutrality equation).

The macroscopic physical quantities associated with the guiding center particles in a volume ΔV are defined as follows. f_i, n_i, m_i, $q_{i\psi}$, and χ_i are the distribution function, density, mass, heat flux in ψ space, and thermal conductivity of the guiding center ions, respectively. Radial particle flux is zero in the present adiabatic electron model. The volume can be defined as a flux shell for a flux surface averaged quantities, or any local cell for local quantities.

$$f_i(X, v_\parallel, \mu) = (1/\pi \Delta V) \sum_{X_j \in \Delta V} w_j \delta(X - X_j)\delta(v_\parallel - v_{\parallel j}\delta(\mu - \mu_j) \qquad (2)$$

$$W = \sum_{X_j \in \Delta V} w_j$$

$$n_i = = W/\Delta V$$

$$u_\parallel = \sum_{X_j \in \Delta V} v_{\parallel j} w_j / W$$

$$T_i = \frac{1}{3} \sum_{x_j \in \Delta V} w_j m_i \left(2B\mu + \left(v_{\parallel j} - u_\parallel\right)^2\right)/W$$

$$q_{i\psi_N} = (1/2) \sum_{X_j \in \Delta V} m_i \left(2B\mu + (v_{\parallel j} - u_\parallel)^2\right) w_j \dot{\vec{X}}_j \cdot \nabla\psi / W$$

$$\chi_i = q_{i\psi}/(|\nabla\psi|^2 \frac{\partial T}{\partial \psi})$$

$$\qquad (3)$$

The following gyrokinetic Poisson equation, or equivalently the quasi-neutrality equation, is solved on the mesh nodes, with the finite $k_\perp \rho_i$ correction to the Pade approximation [24–

26],

$$-\nabla_\perp \cdot \frac{\rho_i^2}{\lambda_{Di}^2}\nabla_\perp\Phi = e\left(1 - \nabla_\perp \cdot \rho_i^2\nabla_\perp\right)(\overline{n}_i - n_e), \tag{4}$$

where $\rho_{\mathbf{i}}$ is the ion gyroradius vector, λ_{Di} is the ion Debye length, the flux-surface-averaged electron density n_e does not respond to the flux-surface-averaged electrostatic potential, and $\overline{n}_i$ is the ion guiding center density at real position $\mathbf{x}$ [27],

$$\overline{n}_i = \frac{1}{2\pi}\int f_i(\mathbf{X}, \mu, u)\delta(\mathbf{X} - \mathbf{x} + \rho_{\mathbf{i}})d\mathbf{X}d\mu d\alpha,$$

where α is the gyro-phase. In the left hand side of Eq. (4), the quantity ρ_i^2/λ_{Di}^2 has radial dependence through the real ion density (= electron density), which is time invariant in the present adiabatic electron model. In the right hand side, ρ_i^2 is function of ion temperature which is radial and time dependent. The above gyrokinetic-Poisson equations are valid for steep gradient plasma, too, as long as the plasma gradient scale length is much greater than the ion gyroradius. In some ITG turbulence simulations, the finite $k_\perp\rho_i$ correction term is neglected since the ITG modes are localized to low $k_\perp\rho_i$ values [2, 3]. However, when the finite $k_\perp\rho_i$ effect becomes important, as in the study of trapped electron modes, this term must be kept [24–26].

A full-f particle simulation solves the $df/dt = C(f) + S$ equation directly in a gyrokinetic form, where C is the collision operator and S is the sources and sinks, by following the guiding center particle motion (1) in 5D phase space in the electric field given by Eq. (4). There is no scale separation in the self-organization between the background and the perturbed plasma dynamics. In return, the simulation is expensive: A full-f gyrokinetic particle-in-cell code requires much more marker particles, roughly by a factor $\sim (n/\delta n)^2$, than a delta-f gyrokinetic code. Fortunately, the simulation can be carried out without suffering from the growth of the random particle weights as in a delta-f code. The disadvantage of the full-f algorithm relative to a delta-f algorithm is thus diminished in a long time simulation (eventually, the weights in delta-f algorithm are bounded). The actual number of full-f marker particles used in this study will be discussed in a later section, together with a discussion on convergence in particle numbers.
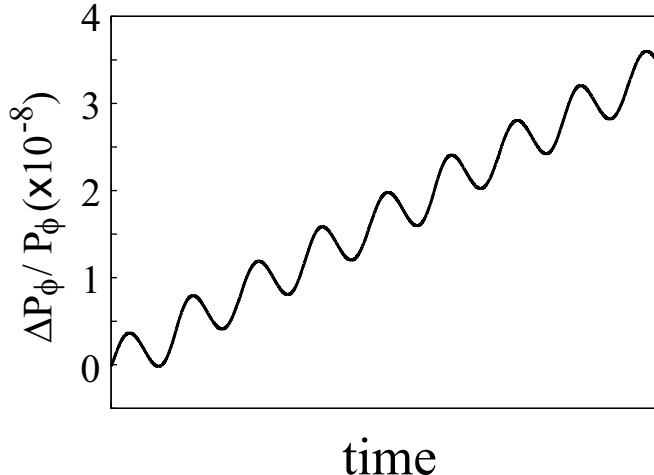
FIG. 1: Relative change in canonical angular momentum P_ϕ from the error in the 3rd order predictor-corrector solution of the Lagrangian equation of motion is on the order 10^{-8} over a significant fraction of a typical turbulence simulation period.

III. BASIC VERIFICATION OF XGC1

Verification is an important part of the code development. It provides evidence that the equations used in the simulation are solved correctly and accurately. We have performed numerous verification exercises on the basic solving capability of XGC1. The first solving capability we need to check is on the collisionless single particle equation of motion (1) as used in the code, for which the canonical angular momentum conservation is an important barometer since it defines the accuracy in the radial particle position during the simulation (energy conservation is about one order of magnitude more accurate than the canonical angular momentum conservation). Correct momentum conservation sets the basis for correct mean radial potential variation and neoclassical heat flux. Figure 1 shows the change in relative canonical angular momentum $\Delta P_\phi/P_\phi$ of a 1 keV trapped ion in the 3rd order predictor-corrector time advance of the Lagrangian equation of motion, Eq. (1), in DIII-D geometry [28]. Each wiggle period represents a banana orbit period ~ 0.1 ms. It can be seen that there is a relative drift of $\Delta P_\phi/P_\phi$ by about 3×10^{-8} in $\simeq 7$ banana orbit periods, which is a few times shorter than a typical turbulence simulation time in XGC1. Using the small $\Delta \psi_N$ approximation $\Delta \psi_N/\psi \sim \Delta r/a$, the simulation system size $a/\rho_i \sim 200$, where a is the plasma minor radius at the magnetic separatrix surface of DIII-D, and a minimal mean field
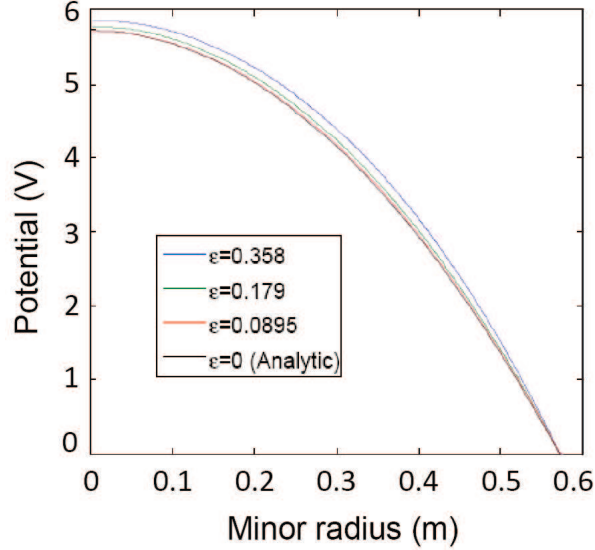
FIG. 2: Rapid approaches of the XGC1 solution to the exact cylindrical solution as the inverse aspect ratio is reduced. At $\epsilon = r/R_0 = 0.0895$ the red (XGC1 solution) and black (exact cylindric analytic) curves are already visually indistinguishable.

radial scale length at $k_r \rho_i \sim 1$ (about 2 cm), the error in the mean potential caused by the erratic drift in the single particle motion in the amount $\Delta P_\phi / P_\phi \sim 3 \times 10^{-8}$ can be easily estimated to be, from Eq. (4), $\delta_{error} e\phi/T_i \sim 10^{-5}$ in $\Delta t \sim 7$ banana orbit periods. Thus, it takes about 7,000 banana orbit times of 1 keV ion (or ~ 0.7 sec) to destroy a physical mean field of $\sim 0.01 T_i$ over $L \sim 2\pi \rho_i$. According to this estimate, the collisionless single particle motions can be regarded to be accurate for mean field evaluation over the radial $L \sim 2\pi \rho_i$ (with $\sim 10\%$ mean field level) up to ~ 700 banana bounce periods (~ 70 ms, which is about 30 times longer than the simulation time performed in the present work) if we can limit the error in the mean potential to be up to $\sim 1\%$. In the actual simulations presented here, we raised the accuracy even higher by using the 4-th order predictor-corrector routine. We note here that the accuracy of the gyrokinetic turbulence simulation, in response to the error in the single particle motion, is significantly raised by the large factor ρ_i^2/λ_{Di}^2 arising from the classical polarization response of the ions (the left hand side of the gyrokinetic Poisson equation 4). Otherwise, $\Delta P_\phi/P_\phi \sim 3 \times 10^{-8}$ could result in a significant error in the ordinary Poisson equation solution.

The global electrostatic potential solver in XGC1 has been verified using a primitive form of the manufactured solution method in a simple analytic concentric circular cross-sectional
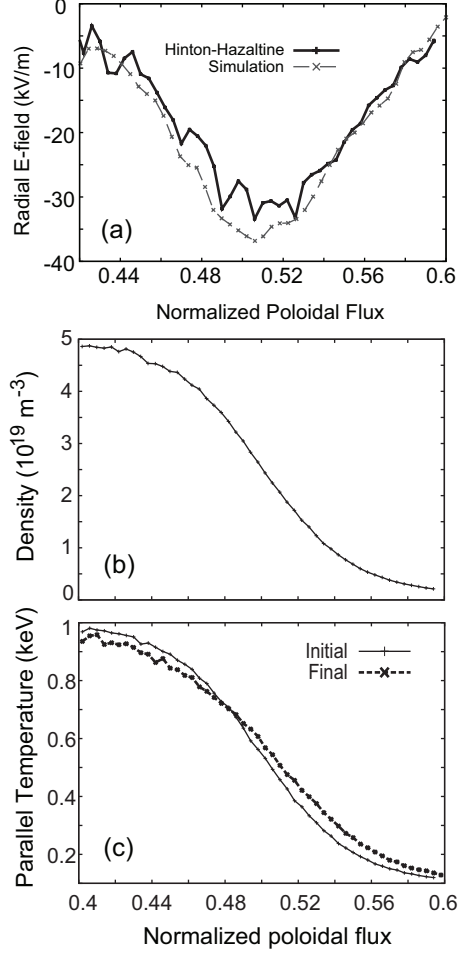
FIG. 3: Verification of the neoclassical poloidal rotation in full-f XGC1 in a realistic DIII-D geometry (g096333.03337). (a) The solid line is the radial electric field E_r obtained when we use the collisionality-dependent analytic formula of Hinton-Hazeltine [29] on the radial plasma profiles from XGC1 and the dashed line with X-mark is what is actually obtained in XGC1. Corrugation on the analytic result is from differentiation of the numerical profile data. (b) Radial profile of particle density and (c) radial profile of initial and final ion parallel temperature from the code. The q-profile is given in Figure 11(b).

toroidal magnetic geometry,

$$\vec{B} = \frac{I}{R}\hat{\phi} + \nabla\psi \times \nabla\phi$$

$$\psi(r) = B_0 \int_0^r \frac{r'}{q\sqrt{1 - r'^2/R_0^2}} dr'$$

where $I = B_0 R_0$, $\hat{\phi}$ is the unit vector in the toroidal angle ϕ direction in cylindrical coordinate

10

system, r is the minor radius, R is the major radius, ψ is the poloidal magnetic flux and B_0 and R_0 are the magnetic field strength and major radius on the magnetic axis, respectively. In this procedure, an analytical solution of the gyrokinetic Poisson equation (4) is obtained for a uniform charge distribution in the limit of infinite toroidal aspect ratio $R_0 \rightarrow \infty$ (i.e., the cylindrical limit). The gyrokinetic Poisson equation in XGC1 is solved using the same uniform charge distribution on the right-hand side. The numerical solution obtained from XGC1 is then compared to the analytical solution for a cylindrical equilibrium, checking the convergence as the toroidal aspect ratio is increased. As can be seen in Figure 2, the solution from XGC1 approaches rapidly to the exact cylindrical solution as R_0 is increased. At $\epsilon = r/R_0 = 0.0895$ the red (XGC1 solution) and black (exact cylindric analytic) curves are already visually indistinguishable.

The collisional neoclassical equilibrium and ion thermal conductivity have been verified. Figure 3 is a verification of the neoclassical poloidal rotation in full-f mode in a realistic DIII-D geometry (g096333.03337) [28], which is the same shot number as that for the turbulence study in the later section (the safety factor q profile is shown there). The solid line is the radial electric field E_r obtained when we apply the collisionality-dependent analytic formula of Hinton-Hazeltine [29]

$$u_{i,\|} = \frac{T_i}{eB_p}\left[k\frac{d\log T_i}{dr} - \frac{d\log p_i}{dr} - \frac{e}{T_i}\frac{d\phi}{dr}\right]$$

to the radial plasma and toroidal rotation profiles from XGC1, and the dashed line is what is actually obtained in XGC1. The collisionality enters into the poloidal rotation factor k. B_p is the poloidal magnetic field strength. Radial profiles of particle density, and initial and final ion temperature are shown together. About 10% level of difference is observed. Considering the approximate nature of the analytic formula, this level of difference is unavoidable in verification. In the neoclassical simulation, the radial temperature (density) varies from 1 keV to 50 eV (5×10^{19} to 1×10^{18} m^{-3}) in the form of hyperbolic tangent over the normalized poloidal flux from 0.4 to 0.6, with the full radial width of 0.1.

Figure 4 is the ion thermal conductivity compared with the Chang-Hinton formula [30, 31]. The XGC1 result agrees with the analytic formula within about 15%. Again, considering the approximate nature of the analytic formula, this level of difference is unavoidable in the verification.

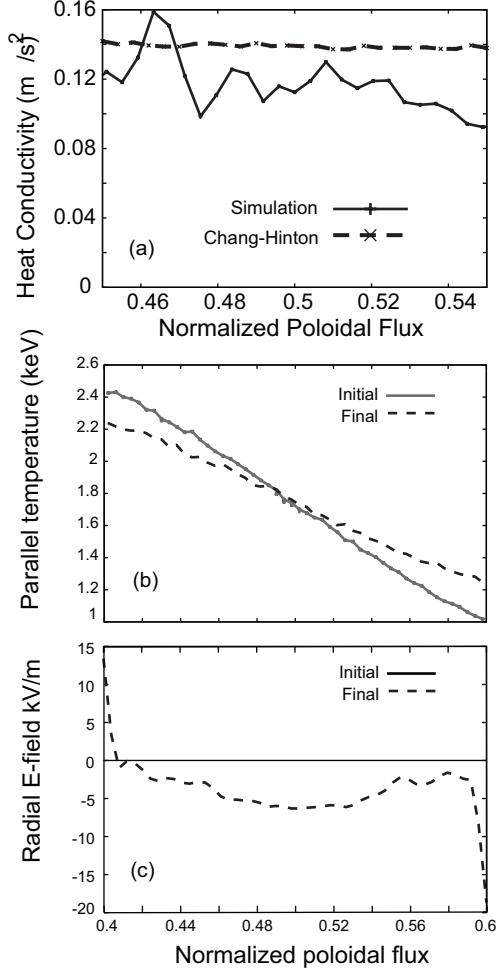The basic turbulence solver capability of XGC1 is verified in delta-f and full-f modes.

FIG. 4: (a) Ion thermal conductivity from XGC1 is compared with the Chang-Hinton formula [30, 31]. (b) Initial and final parallel temperature profile and (c) radial electric field from the simulation are shown together. Concentric circular flux surface is used for this study with q=2 and a flat density $5 \times 10^{19} m^{-3}$. The radial electric field quickly establishes an ion orbit time and stay steady during the temperature relaxation.

In Fig. 5, the dependence of GAM (geodesic acoustic mode) damping rate on the safety factor q is compared with a known analytic theory in delta-f mode [33], as well as other code results (quoted from Ref. [32]). A satisfactory result from XGC1 (red diamond) can be seen. Collisionless residual potential agrees well with the analytic result of Hinton and Rosenbluth [34] (see Fig. 6). In Fig. 6, the time in the horizontal axis is normalized to the toroidal transit time of a 1 keV ion along the magnetic axis. The linear ITG growth rate and the real frequency from XGC1 in delta-f cyclone plasma (Fig. 7a) is compared against the
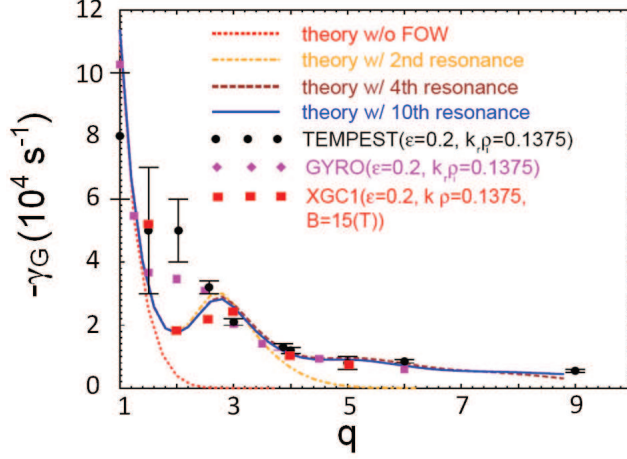
FIG. 5: Damping rate γ_0 of GAM versus the safety factor q in comparison with a known analytic theory in delta-f mode (quoted from Ref. [32]), demonstrating a satisfactory result from XGC1 (red diamond).
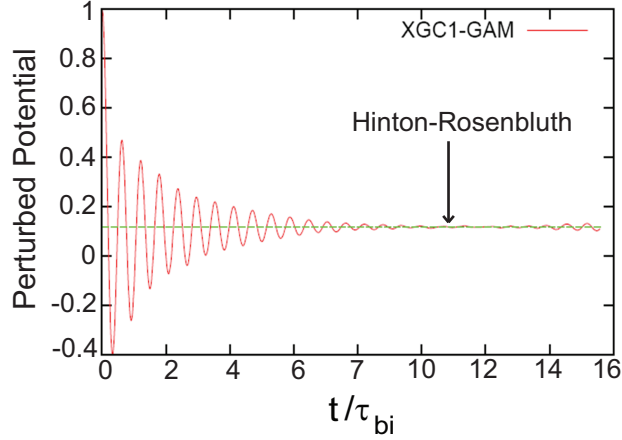

FIG. 6: Collisionless residual potential from GAM oscillation in XGC1 agrees well with the analytic result of Hinton and Rosenbluth [34]. Safety factor q=1.5 is used in this study and $\tau_{bi} = 2\pi R/\sqrt{2}v$, where $v = (kT_i/m_i)^{1/2}$.

results from the linear eigenvalue code FULL[35, 36] and the global core gyrokinetic particle code GTC (Fig. 7b) [37] in the global cyclone geometry with $R/L_T = 6.9$. In XGC1, a Gaussian smoothing has been used on the poloidal plane, with the Gaussian width $\simeq 1.5\rho_i$. The results in Fig. 7 show reasonably good agreement with FULL code study and Ref. [37], and equally well with other benchmarking studies reported in Ref. [19].

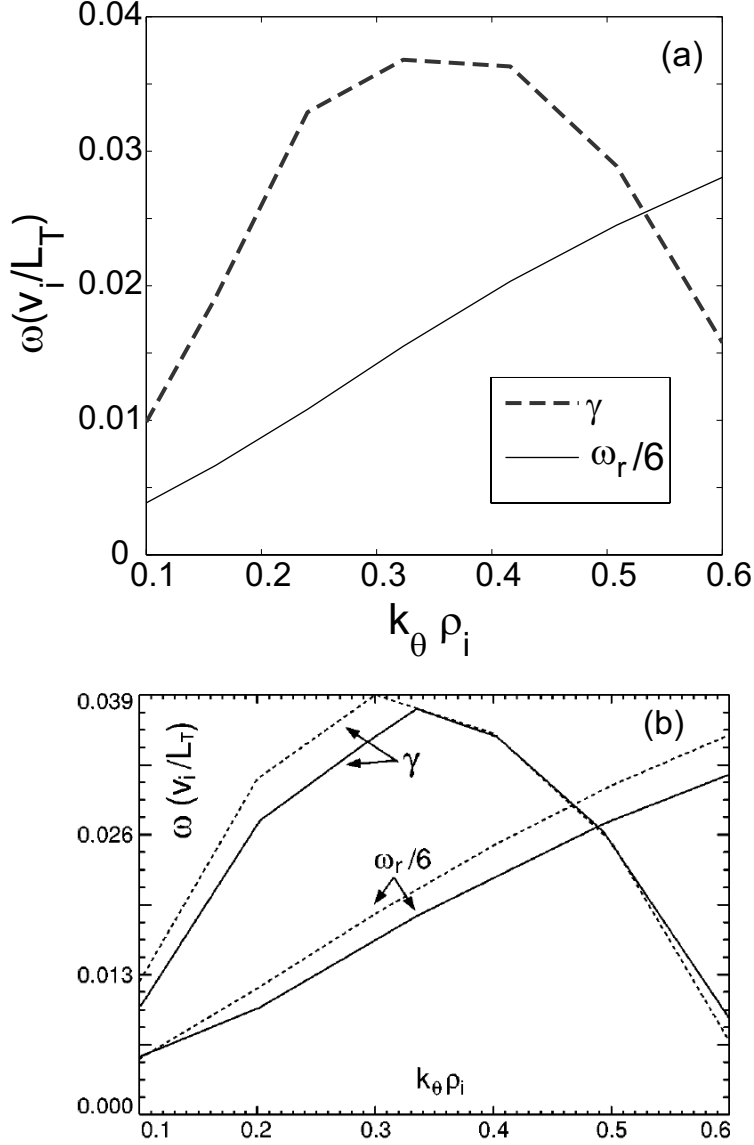Figure 8 shows comparison of the collisionless delta-f ion thermal conductivity χ_i behavior

13

FIG. 7: The linear ITG growth rate and the real frequency from (a) XGC1 in delta-f cyclone plasma is compared against the result from (b) the linear eigenvalue code FULL[35, 36] and a gyrokinetic particle code GTC [37] in the global cyclone geometry with $R/L_T = 6.9$. The results shown here compare equally well with other benchmarking studies reported in Ref. [19].

in time, between XGC1 in delta-f mode and the delta-f GTC in the global cyclone geometry. The heat source is turned off in the comparison since two codes use physically different heating methods. For both codes use Monte Carlo algorithms, two turbulence solutions can only be compared in a statistical sense. The agreement is reasonable. Sourceless χ_i from both codes decays at later time from the profile relaxation effect.
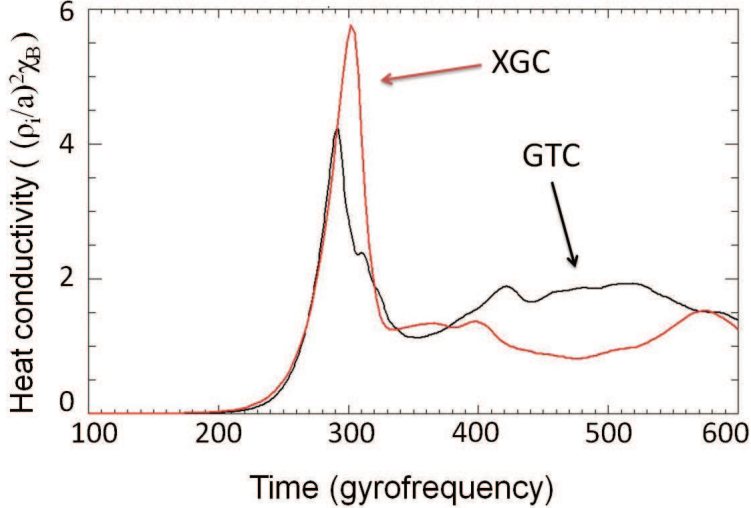
14

FIG. 8: Comparison of the delta-f ion thermal conductivity χ_i behavior in time, between XGC1 in delta-f mode and the core gyrokinetic particle code GTC in the global cyclone geometry.

After the verification of XGC1 in the conventional delta-f turbulence mode[38], the full-f solution is compared with the delta-f solution. For this comparison, we used the full capability delta-f mode, as was used in the comparison performed by Idomura[2], without the conventional simplification. The heat source and collision are turned off for this comparison. As can be seen in Fig. 9, the comparison shows reasonable agreement between the delta-f and full-f modes. Both the heat conductivity and the R/L_T show reasonable convergence to each other.

With these verifications ranging from single particle motion, to collisional neoclassical physics, and to the GAM and linear/nonlinear ITG physics in delta-f mode, we present the full-f simulation of ITG turbulence in a realistic geometry. We note here that the verification exercises presented here are by no means complete. Continuous verification exercises are to be performed, and new verification methods are under development. There are also a few global full-f turbulence codes being developed in the global fusion community [2–4]. Quantitative comparison of specific full-f solutions among these codes have not been attempted yet, but to be performed in the near future.
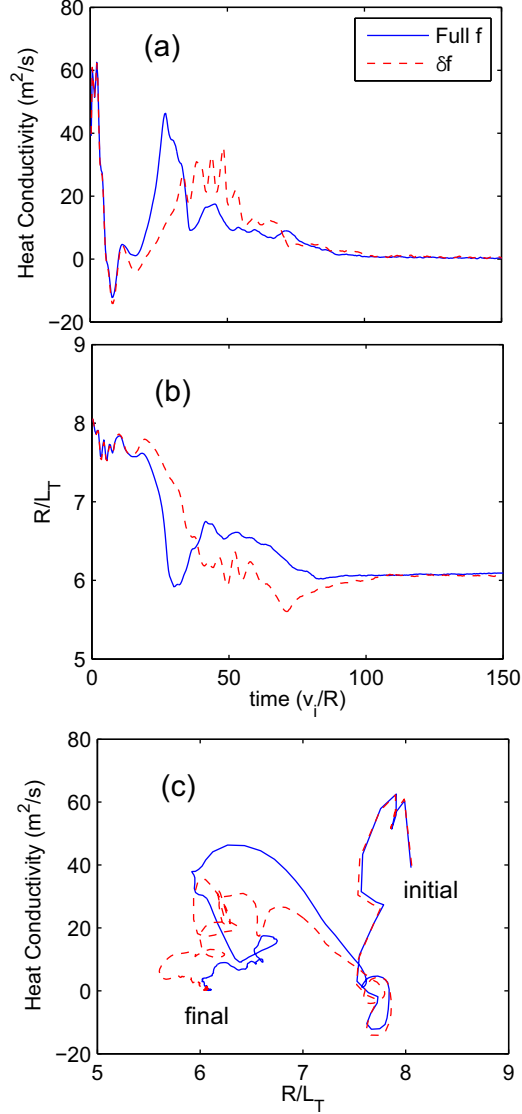
FIG. 9: Comparison of XGC1 between the delta-f and full-f modes.(a) Heat conductivity change in time, (b) R/L_T change in time, and (c) Heat conductivity vs. R/L_T are plotted. Both the heat conductivity and the R/L_T show reasonable convergence to each other.

IV.   FULL-F SIMULATION OF GLOBAL ITG TURBULENCE IN XGC1

We load the marker particles initially as a local Maxwellian, with flux-function density and temperature profiles. Instead of using the marker particle density to describe the radial profile of plasma number density, we use the particle weight distribution in radius. To be more specific, the particle weight distribution w_j in Eq. (2) is initialized with ψ_N dependence. This method can resolve the enhanced particle noise problem at the low density region of

16

the plasma profile. We note here that the local Maxwellian loading in the laboratory frame contains some unspecified initial toroidal rotation in an inhomogeneous plasma, which is physically insignificant compared to other free energy (such as radial pressure gradient). Thus, the effect of initially large toroidal rotation on turbulence cannot be studied in the present simulations. A neutral beam type of external momentum source is not considered in the present work either, even though this capability is available in the other XGC family code, XGC0.

We could also initially load the marker particles as a non-local canonical Maxwellian, which may yield more rapid reduction of the initial GAM activities and faster self-organization to neoclassical solution [39], hence an easier growth of turbulence. It is well-known that unless the initial GAM activities are subdued, ITG turbulence does not grow in a full-f simulation [40]. However, the canonical Maxwellian loading has a disadvantage in that it is difficult to customize the radial temperature and density profiles. In spite of the obvious disadvantage from the longer initial neoclassical equilibration time, we choose the local Maxwellian loading to take advantage of the easier profile customization. We get compensation for the disadvantage by obtaining a neoclassical radial electric solution in a pre-condition simulation and use it in the turbulence simulation as the initial electric field. Since the initial particle loading is still local Maxwellian, this process does not eliminate the initial GAM oscillations completely, but helps reduce the amplitude and the relaxation time.

The boundary condition we use on the elliptic Poisson equation is that the electrostatic potential on the separatrix surface $\psi_N = 1$ vanishes. Particle simulation volume is bounded by $\psi_N = 0.9$. Any particle leaving the surface $\psi_N = 0.9$ returns back to $\psi_N \leq 0.9$ along the collisionless neoclassical orbit (reflection condition with the proper orbit information). Physical phenomena are studied at $\psi_N \leq 0.8$, away from the reflection boundary.

Initial plasma profiles are shown in Fig. 10. The initial ion temperature T_i at the magnetic axis is chosen to be 4.5 keV, dropping to 1 keV at the simulation outer edge ($\psi_N = 0.9$, assumed to be near the pedestal top) with linear dependence in the real radius at outside midplane. Relation between the real distance along the outside midplane and ψ_N is given in Fig. 11, together with the safety factor q profile. These T_i values are not far off from experimental observations, hence representing realistic ratio of the ion larmor radius (or turbulence wave length) to the device size ($a_{0.9}/\rho_i \simeq 180$ where $\rho_i \simeq 3$ mm is the average

ion gyroradius and $a_{0.9} \simeq 53$ cm is the minor radius at $\psi_N = 0.9$). Of course, the initial T_i profile changes in accordance with the transport as the simulation progresses. For a representative $v_i = (T_i/m_i)^{1/2}$, where m_i is the deuteron mass, we take $T_i = 4$ keV. Notice here that the increase of R/L_T with radius indicates that the turbulence drive is stronger at higher minor radius.

Plasma density at the magnetic axis is chosen to be $6 \times 10^{19} m^{-3}$, dropping to $4 \times 10^{19} m^{-3}$ at $\psi_N = 0.9$ with linear dependence in $\sqrt{\psi_N}$. Since we use adiabatic electrons, the real plasma density profile does not change in time. The temperature and density profiles are within a realistic range of experimental values in DIII-D. However, in order to save the computing time, we artificially enhance the collision frequency by factor of 10 (yielding the average ion collision time to be $\tau_{ic} \simeq 140\ v_i/R$). The simulation is then performed to a few to several collision times. Not only the neoclassical relaxations, but also the GAM and zonal flow relaxation become faster in proportion to collision frequency. Factor of 10 enhancement of the collision frequency still keeps the plasma in the banana regime even at the simulation outer boundary ($\nu_* = 0.9$ at $\psi_N = 0.9$), keeping the integrity of the particle orbit dynamics.

Figure 12 shows convergence in marker particle number from the full-f XGC1 test runs in a DIII-D sized circular geometry with the radial heat-flux driven by 2MW of central heating. Ion thermal conductivity χ_i appears to show converged behavior at later time for an average 800 particles per grid node. However, R/L_T in Fig.12b shows that 800 particles per node is not enough and that 1,600 particles per node is reasonable. Convergence tests in the real simulation geometry shows a similar feature. Use of an average $\sim 2,000$ marker particles per grid node (total of 3.1 billion marker particles) is reasonable for the present global ITG turbulence. This yields the noise driven χ_i at the level $\simeq 0.05\ m^2/s$, which is identified from a simulation performed without ITG or collisions. In the actual simulation presented here, we raised the particle number to average 3,000 per grid node (corresponding to total of 4.7 billion marker particles. The maximal number of particles used for convergence test was to 12 billion particles.). The neoclassical thermal conductivity level $\chi_i \simeq 0.7\ m^2/s$ and the combined turbulence-neoclassical thermal conductivity level $\stackrel{>}{\sim} 1.5 m^2/s$ from the actual simulations (see pictures later) are much above the noise level. Convergence test in the grid size shows that we need $\simeq 3\ mm$ average grid size at the outside midplane, which is the average ρ_i and which is what we use in the actual simulations. A simulation takes about 20
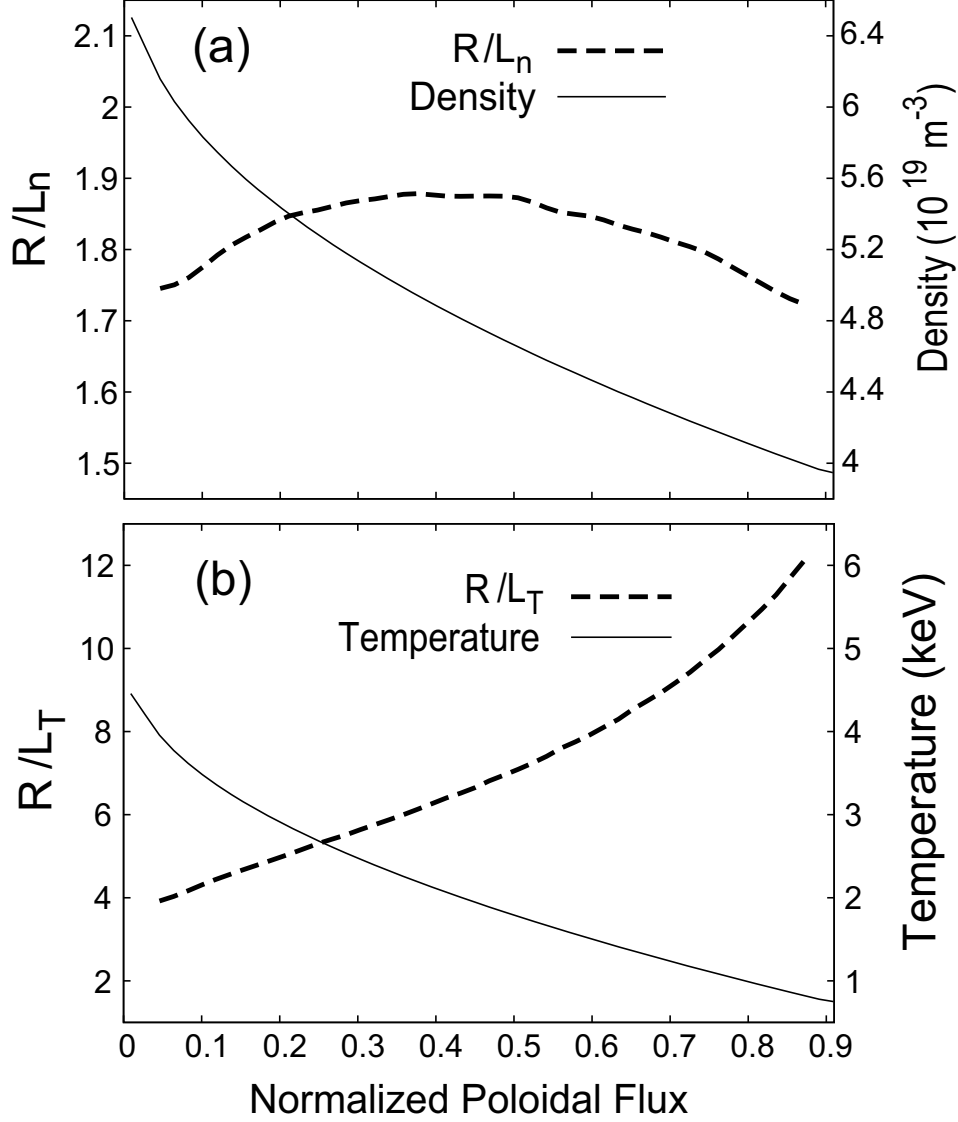
FIG. 10: Initial plasma density and temperature profiles. Electron temperature is assumed to be equal to ion temperature. Gradient scale lengths relative to the major radius on magnetic axis are shown together.

hours on 59,904 CRAY XT5 cores to reach the self-organized quasi steady state and another 10 hours to confirm that the final state is reasonably out of the initial transient state (total simulation period corresponds to 2.34 ms in real time).

4.5MW of total heat is added around the magnetic axis ($\psi_N \leq 0.04 \simeq 10cm$) to force a heat flux into the turbulence region. Heating is achieved by raising the particle energy uniformly in the heating region by a small fraction of kinetic energy while keeping the pitch angle invariant. This rate of heating in a small central volume is too large for the local ITG
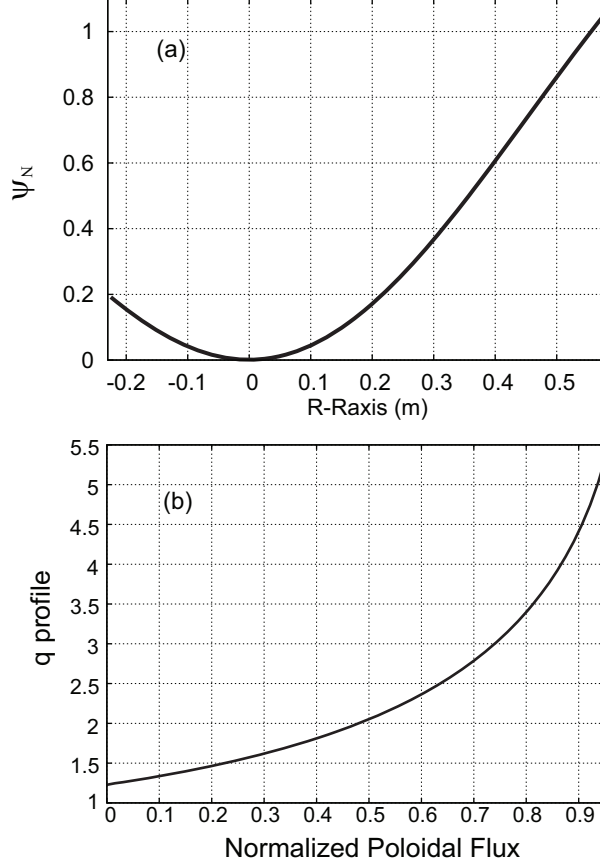
FIG. 11: (a) Relationship between the normalized poloidal flux ψ_N and real distance in meters from the magnetic axis (at R_{axis}) to the flux surface (at R) along the midplane. (b) Radial profile of the safety factor q.

and neoclassical transports to efficiently transport the heat radially outward. As a matter of fact, the full-f plasma even shows resistance to the local heat flux by developing a strong $E \times B$ shearing rate in the heat source region (relation of this observation to the internal transport barrier formation in a reversed magnetic-shear configuration is to be investigated in the near future). In order to ensure a smooth outward heat flux from the localized heating, we inject a strong local collisional neoclassical transport by further increasing the Coulomb collision rate by another factor of 10 in the central core ($\psi_N \leq 0.08 \simeq 13cm$) somewhat greater than the heat source volume.

An explicit heat sink model is not used in the present simulation. Instead, we use the outer low temperature region as a heat absorption layer and exclude the outer simulation layer ($0.8 < \psi_N \leq 0.9$) from the physics study volume. As a result, the ion temperature
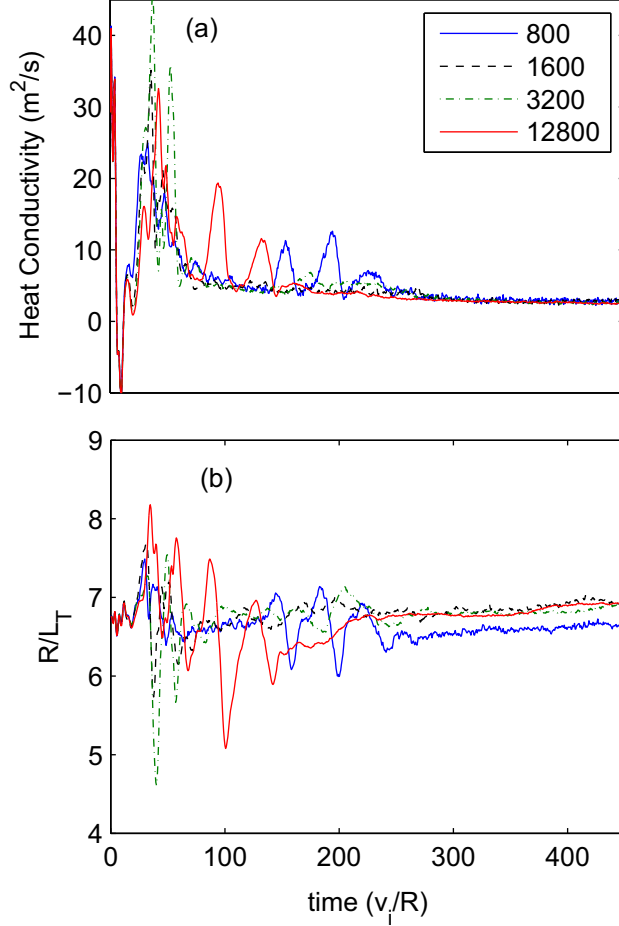
FIG. 12: (a) Representative χ_i results from convergence tests in marker particle numbers (average 800, 1,600, 3,200, and 12,800 particles per node). It appears to be that 800 particles per node might be good enough. However, (b) test of R/L_T shows that at least 1,600 particles per node is needed.

gradient around $\psi_N = 0.9$ flattens somewhat in a short time turbulence simulation. We find that this "heat absorption layer method" is adequate to sustain heat flux across the $\psi_N = 0.8$ surface for the duration of the present simulation.

Figure 13 shows the time behavior of effective ion thermal conductivity (thermal flux divided by local T_i gradient), together with the fluctuating potential squared $((\delta\Phi)^2)$, from the start of the simulation across $\psi_N = 0.45$ which corresponds to r/a=0.6 on the outside midplane with the plasma minor radius "a" defined to be the magnetic separatrix surface. The short initial jittering is driven by the GAM oscillations during the toroidal self-organization of the radial electric field, ion distribution function, plasma profile, and toroidal rotation in
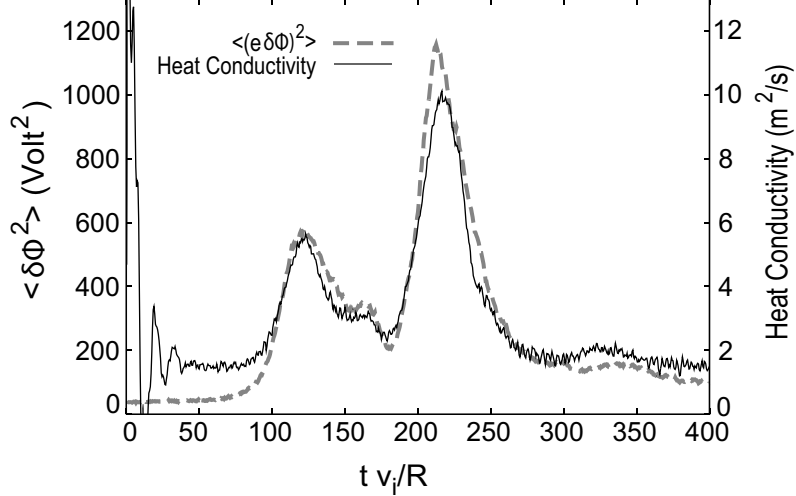
FIG. 13: Time behavior of the effective ion thermal conductivity and the turbulence amplitude squared in MKS unit across the $\psi_N = 0.45$ surface.

the initial local Maxwellian loading. As the large initial GAMs settle down,ITG modes start to grow at about 75 v_i/R. As mentioned in the previous section, it is well-known that unless the large jittering from the initial GAM activities is subdued, ITG turbulence does not grow in a full-f simulation [40]. The total simulation time is about four times the collision time.

We note here that the initial settling down of the system before the growth of ITG is yet far from neoclassical equilibrium. The thermal conductivity between 30 and 75 v_i/R is greater than the steady state neoclassical value of the system [30, 31]. Figure 14 is the neoclassical ion thermal conductivity of the system and the total turbulent-neoclassical ion thermal conductivity at the relatively steady final stage.

Figure 13 also shows that there is a large multiple bursts of low-frequency heat flux in the initial stage of nonlinear turbulent transport until about 250 v_i/R, as the initial ion temperature profile and the turbulence begin to self-organize, followed by a relatively steady level of heat flux behavior at later time. The inter-burst period is much greater than the initial GAM jittering period. Since the transient bursty stage shows interesting relation of E×B shearing dynamics to the radial heat burst, we discuss the bursty and relatively steady stages separately. Figure 15 displays the contour plot of two dimensional electric potential $\delta\Phi = \Phi - \Phi_{0,0}$ on a constant toroidal angle plane (called poloidal plane) in the bursty stage at t=200 R/v_i.

Figure 16 is the 2D contour plot of (a) the E × B shearing rate strength, (b) the radial
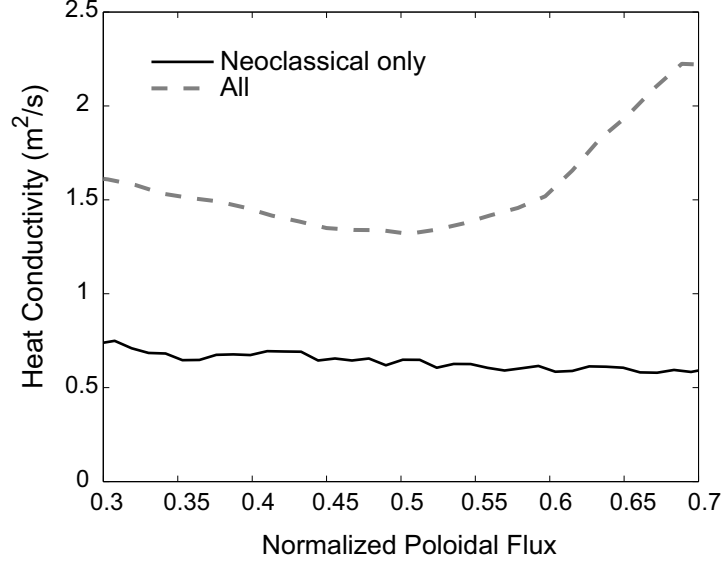
22

FIG. 14: The neoclassical ion thermal conductivity of the system (solid) and the total turbulent-neoclassical ion thermal conductivity (dashed) at the relatively steady final stage.
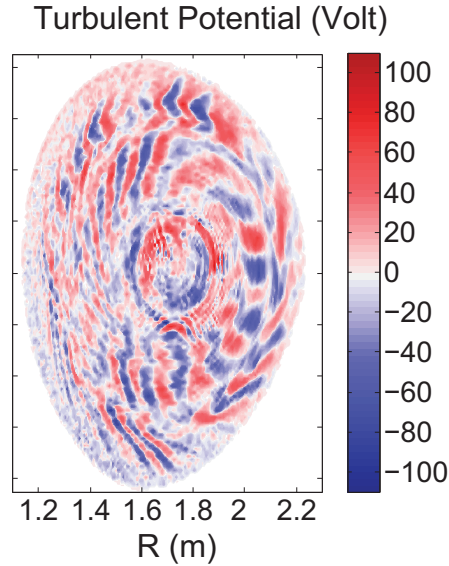

FIG. 15: Two dimensional electric potential contour for $\Phi - \Phi_{0,0}$ on a constant toroidal angle plane in the middle of the bursty nonlinear relaxation stage.

heat flux strength in the ψ_N-time space, and (c) the quasi-steady state E × B shearing rate. Simulation lasts for another 200 R/v_i. Figure 13 and 16 are cut off at t=400 R/v_i to enhance visual efficiency since the quasi-steady does not have much variation. Red color signifies the high strength region. Radially outward ballistic heat burst contours are marked with dotted
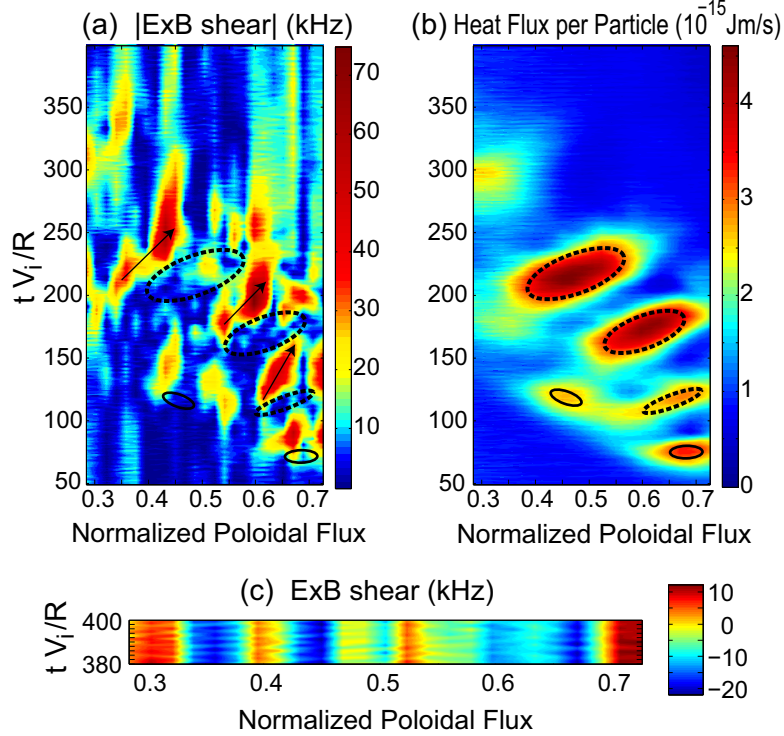
FIG. 16: 2D contour plot of (a) $E \times B$ shearing rate strength, (b) bursty heat fluxes and (c) $E \times B$ shearing rate in the beginning of the steady turbulence stage.

ellipses in both figures for visual guide. Ellipses with solid line denote the heat flux during the initial inward propagation of turbulence front from $\psi_N \simeq 0.7$. We see that a radially outward heat burst flows through the openings of the zonal $E \times B$ shearing barriers until the opening narrows. We also see that the $E \times B$ shearing barrier tends to tilt (visually aided by arrows) toward the outward ballistic heat bursts from the vertical zonal flow direction. However, the tilt angle (=radial ballistic speed) of the $E \times B$ shearing is not as strong as the heat flux, indicative of the natural tendency for the $E \times B$ flow to form radial zonal flow structures. This difference eventually leads to destruction of the phase difference between the $E \times B$ shearing and the heat flux, and stops the bursty train.

The radial size of a burst and the inter-burst distance is ~ 5 cm ($\sim 15\rho_i$, where ρ_i is the local gyroradius). After the bursty behavior is subdued the zonal flows become steady, as can be seen in Fig. 16(c), but decaying in collision time scale [34] as will be more clear in Fig. 17. Figure 17 shows the phase lag and interplay between the heat flux ($\propto$ turbulence intensity) and the $E \times B$ shearing strength at $\psi_N = 0.45$. The decay time of the $E \times B$ shearing is $\sim 50R/v_{i,0.45}$ (a few kHz), where $v_{i,0.45}$ is the local ion thermal
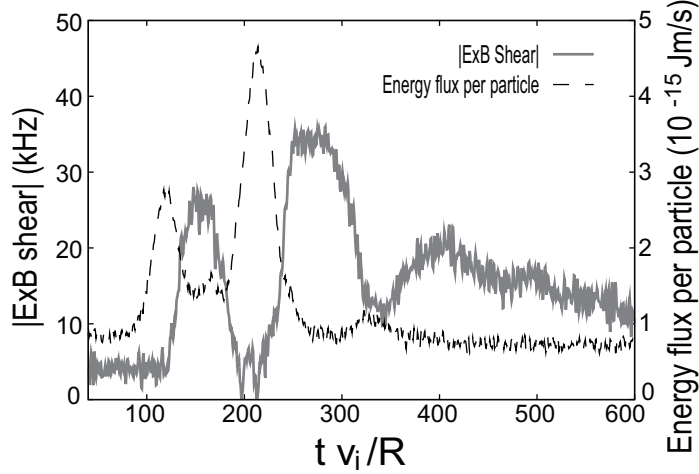
24

FIG. 17: Out-of-phase time behavior between the heat flux and the E × B shearing strength at $\psi_N = 0.45$.

speed at $\psi_N = 0.45$. This decay time is not correlated with GAM frequency or collision time. It is much slower than the GAM oscillation time and faster than the ion collision time. After the first peak in the heat flux decays, the second peak appears after about twice the E × B shearing decay time. The radial speed of the ballistic motion of heat burst is about $V_r \simeq (1/5)\rho_i v_i/R \simeq (1/30)\,\rho_i v_i/L_T$, which is either similar to the analytic intensity burst estimates reported in Refs. [41] or somewhat smaller [42, 43]. Distinction between the $\rho_i v_i/R$ and $\rho_i v_i/L_T$ scalings in V_r is difficult to determine in the present simulation since R/L_T quickly self-organizes to a roughly fixed value $\simeq 6.5 - 7$.

The bursty heat flux, regulated by the zonal E × B shearing, continues until the resulting temperature profile is roughly consistent with the turbulence (and total transport). The large bursty behavior stops and the self-organized state is reached and maintained. In the self-organized state, the local ExB shearing rate (zonal flow) continues to damp [34]. The present study does not give answers to the final saturation of the zonal flow in a collisional full-f simulation because the simulation is not carried out long enough for it. This is another area of focused study in the future. The global ExB shearing rate is maintained by the global E_r profile. This is consistent with the turbulence self-organization with the global mean profile, which is driven by both neoclassical and turbulent physics. The bursty heat flux observation may have some similarity to a previous study reported in the literature[44]. Relation of the present bursty relaxation to the edge localized mode relaxation of overly
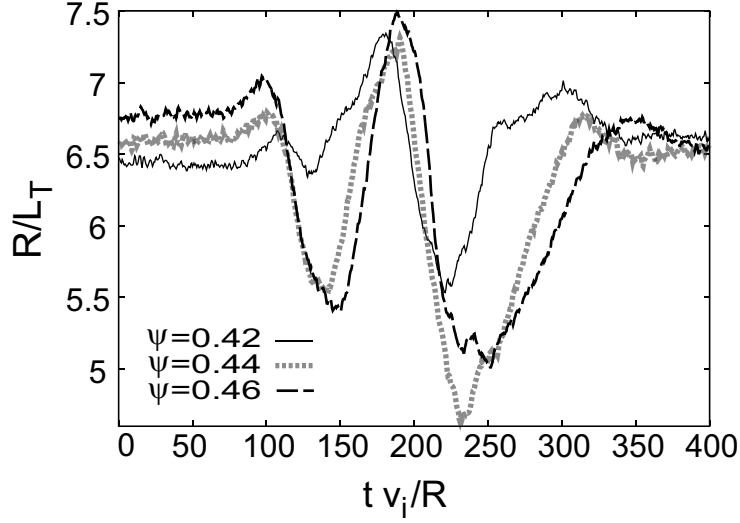
25

FIG. 18: Temperature gradient behavior in time at three adjacent radial locations.

steep pedestal pressure gradient and blob formation is an interesting subject to be studied later.

Figure 18 shows the resulting local temperature gradient behavior in time at three adjacent radial locations. The first group of peaks shows local rise of T_i at the inner radius side of the inward-propagating turbulence front. This corresponds purely to the inward arrival of turbulence intensity front from. Radially outward ballistic motion of temperature gradient is not seen. The second group of peaks corresponds to the large bursty heat fluxes, showing the ballistic outward movement of the temperature gradient. The third group of peaks is weaker, followed by the quasi-steady self-organized temperature gradient.

In the central core, the collisional damping of E × B shearing is offset by the continuous drive from the heat source, and the strong E × B shearing is maintained (see Fig. 15). As a result, the bursty heat flux does not appear there. This phenomenon is not well understood. Possible relation of this phenomenon to the transport barrier formation by localized ion heating is another interesting topic to be studied in the future, especially in a reversed-shear magnetic equilibrium.

Figure 19 shows the frequency spectrum of the heat flux in the middle of the simulation radii at $\psi_N = 0.3$ in the bursty stage (t=120-300 R/v_i) and in the approximately steady stage (t=400-600 R/v_i). It can be seen that the approximately steady-stage satisfies the avalanche statistics of $1/r$, except the GAM influence between ~ 50 and 100 kHz. The large scale bursty stage is characterized by extra intensity in the low frequency below 5 kHz
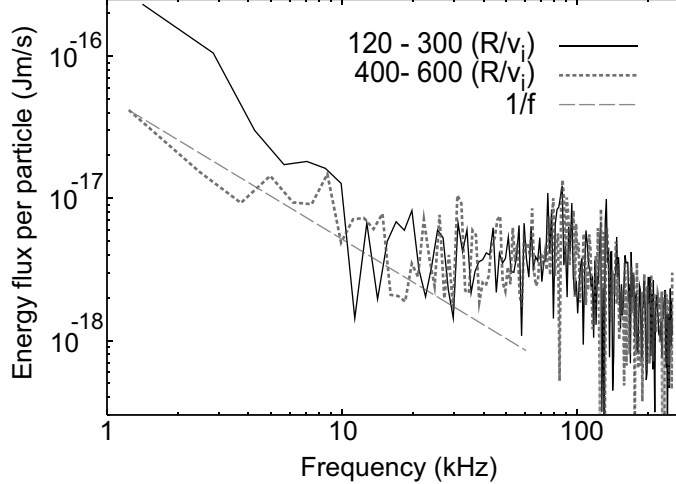
FIG. 19: Frequency spectrum of the heat flux in the middle of the simulation radii ($\psi_N = 0.3$) in the bursty stage and in the final quasi-steady state.

during the bursty stage. In the avalanche stage the bursty heat flux is now part of the avalanche process. Smaller scale bursts may still show up in a longer simulation within the 1/f avalanche statistics. GAM activities are common to the bursty and avalanche phases. It is our speculation that the heat-source driven enhanced turbulence activity in the central core may continuously drive GAMs in the core. An in-depth study is needed for a conclusive insight into the GAM activities in relation to the strong heat flux. The GAM activity is higher at larger minor radii, as can be expected.

Self-organization of the temperature gradient (R/L_T) profile in the turbulent plasma is shown in Figure 20(a). The "final" self-organized R/L_T profile stays approximately unchanged around $R/L_T \sim 6.5 - 7$ during the turbulence evolution over the whole turbulence radii except in the central core region. The self-organized adjustment of the radial ion temperature itself is shown together in Fig. 20(b). Since the needed temperature adjustment amount is small, R/L_T profile is a better barometer of self-organization. In other simulations with heat input as low as 1 MW and as high as 10 MW, the saturation profile of R/L_T is visually indistinguishable in the turbulence region from the 4.5 MW case shown here, suggesting that the self-organized ion temperature profile is "stiff" with respect to the heating strength. What will happen to the stiffness property when the plasma density is also allowed to change is of interest, and is to be investigated in the future when we improve the electron model in XGC1.
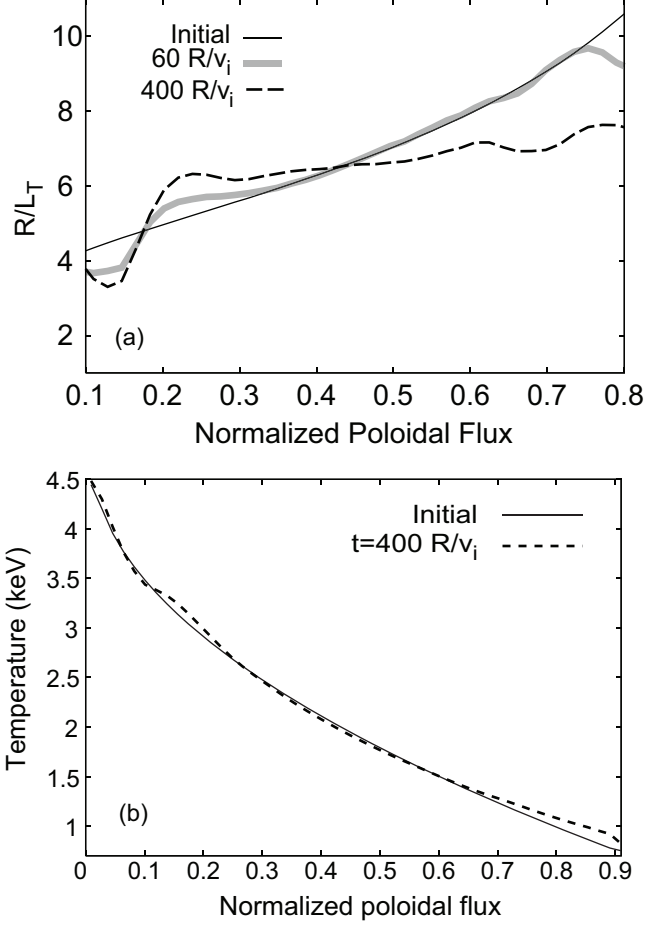
FIG. 20: (a) R/L_T profiles are drawn at the initial, after the initial settling down before turbulence, and in the self-organized stage near the end of the simulation. (b) Comparison between the initial and final ion temperature profiles. The self-organized ion temperature profile becomes stiff in variation of heat source strength.

The global linear ITG stability boundary in the present magnetic geometry has been investigated by running XGC1 in delta-f mode with the zonal flows turned off. As can be seen from Fig. 21, the global growth rate becomes negligible at $R/L_T < 4.6$, then approaches marginal stability at $R/L_T = 4$. It can be seen from the figure that the nonlinearly self-organized temperature gradient at $R/L_T \sim 6.5$ is in a strong linear instability regime.

Figure 22 shows the radial variations (shearing) in the mean E × B flow speed by the turbulence activities. A larger scale ExB flow speed variations can be seen during the bursty phase, followed by smaller scale variations in the avalanche state.

Figure 23 shows the radial correlation length of (a) $E_{r(0,0)}$ and (b) the turbulent com-
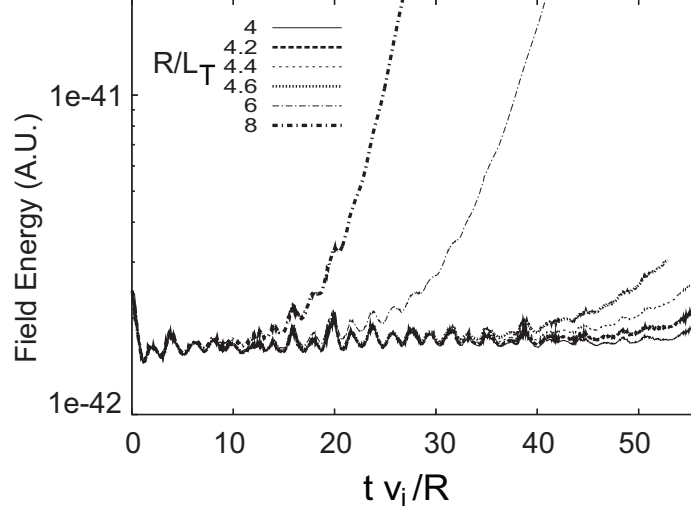
FIG. 21: Growth of linear ITG mode for different values of ion temperature gradient R/L_T in the DIII-D geometry. ITG approaches marginal stability at $R/L_T = 4$ and ITG at $R/L_T \sim 6.5$ is strongly unstable linearly.
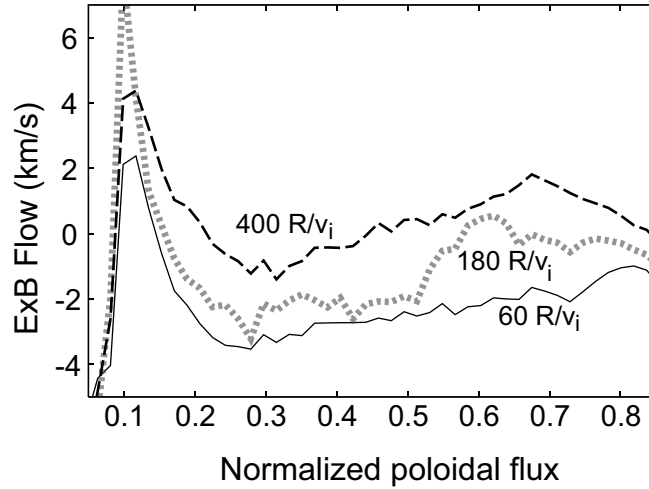

FIG. 22: $E_r \times B$ poloidal rotation speed profile in ψ_N at three different times: after the large amplitude GAM jittering before the turbulence generation ($60R/v_i$), in the middle of the bursty turbulence phase ($180R/v_i$), and during the avalanche phase ($400R/v_i$).

ponent δE, respectively, during the bursty (100-300 R/v_i) and avalanche (300-400 R/v_i) transport phases. Both axisymmetric and non-axisymmetric turbulence exhibit strong correlation over the distance $\lesssim 1$ cm. The strong correlation distance of δE is shorter than that of $E_{r(0,0)}$'s, as expected. The main difference between them is in the residual, long range correlation strength. Unlike δE, the axisymmetric modes have a significant residual
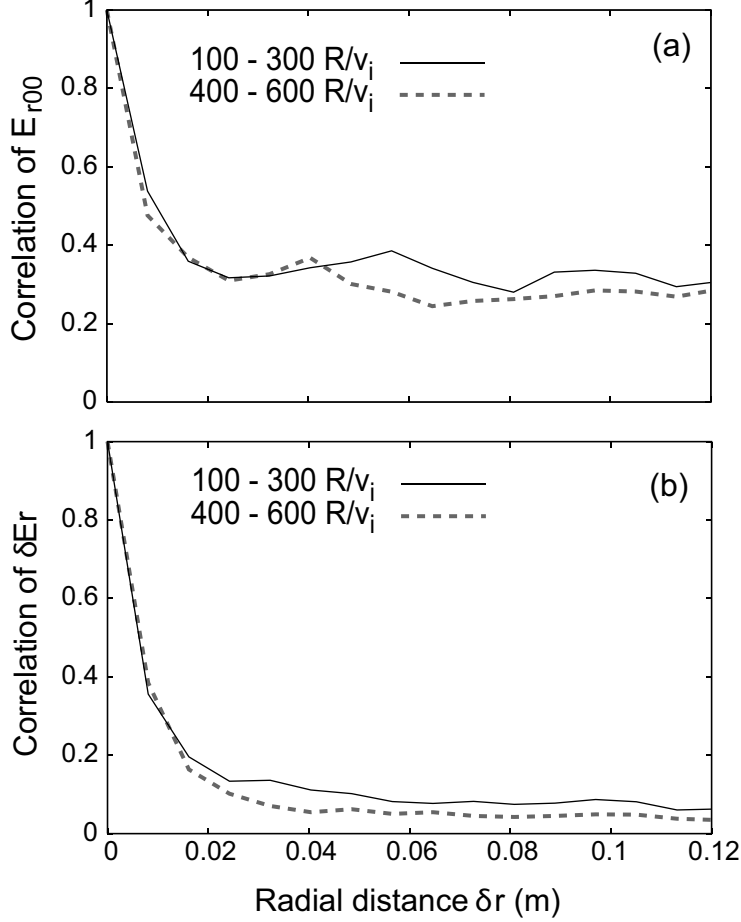
FIG. 23: Radial correlation length of (a) $E_{r(0,0)}$ and (b) δE_r turbulence activities during the bursty (100-300 R/v_i) and steady (400-600 R/v_i) turbulence transport activities.

global correlation, which is not surprising since $E_{r(0,0)}$ in the present full-f simulation contains both mean and neoclassical component. At the same time, it can be noticed that there are extra long range $E_{r(0,0)}$ correlations in the bursty phase, which is consistent with the time dependent ExB shearing as discussed for Fig. 16. On the other hand, δE does not show an obvious sign of this extra correlation in the bursty phase. Detailed study of cross-correlations between the turbulence and heat flux with varying degree of collisions and axisymmetric zonal/mean flows [45] have not yet been performed.

Energy conservation has been investigated within the volume $0.3 \leq \psi_N \leq 0.7$. In Figure 24, total energy flowing into the volume across the inner surface $\psi_N = 0.3$ is shown in solid black line. Sum of the particle energy change, field energy created and out-flowing energy across the outer surface $\psi_N = 0.7$ is shown in blue dashed line. Sum of black and
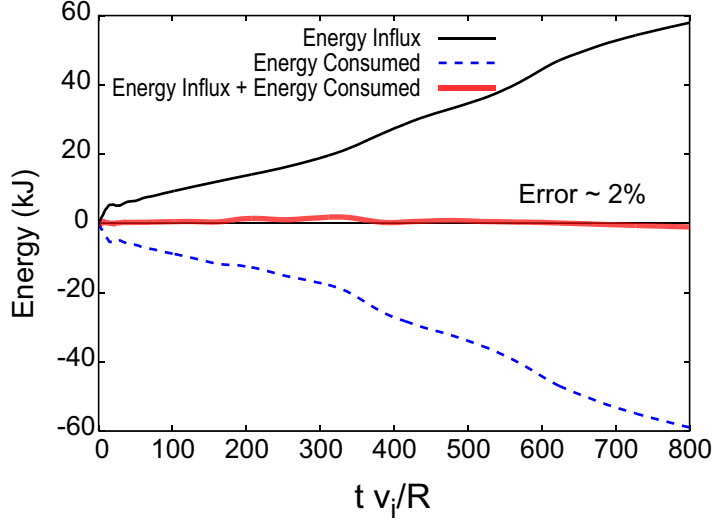
FIG. 24: Energy accounting within $0.3 \leq \psi_N \leq 0.7$ between the total influx across the inner boundary (black curve) and the sum of the consumed energy (blue curve) to the particles, the electric field, and across the outer boundary. Red line shows sum of black and blue curves. About 2% error is noticed. Unlike in a delta-f particle code, error in a full-f code does not grow in principle since the particle weights do not grow.

blue lines is shown in red line, which is supposed to trace to zero line in a perfect energy conservation. This simulation shows about 2% error in the total energy conservation. What is to be noticed here is that unlike in a delta-f particle code where the particle weights grow, the energy conservation error in a full-f code should not grow unless numerical errors grow.

V. CONCLUSIONS AND DISCUSSIONS

The XGC1 full-f gyrokinetic code has been used to study the global ITG turbulence from the magnetic axis to edge pedestal top ($\psi_N = 0 - 0.9$) in a realistic DIII-D magnetic geometry. Electrons are assumed to be adiabatic. Central heating is used to provide radial heat flux in the turbulent transport. A particle number, momentum and energy conserving Monte-Carlo collision operator is used to produce proper collision effects in neoclassical and turbulence physics. Collision frequency is artificially enhanced by factor of 10 to speed up the equilibration and save computing time. XGC1 has been developed to include the magnetic axis, the diverted magnetic field and the material wall geometry, and designed to run on massively parallel high performance computers. Simulations across the magnetic

31

separatrix in DIII-D geometry from $\psi_N \simeq 0.7$ to the material wall has recently been reported elsewhere [8]. The next major goal is a wall-to-wall simulation of the whole plasma to study the core-edge ITG interactions and turbulence spreading.

XGC1 simulation with a strong central heating (4.5MW within r $\leq$ 10 cm) shows that the ion temperature gradient self-organizes around $R/L_T \sim 6.5 - 7$ in the turbulent region, which is above the linear and nonlinear stability limit. The temperature gradient profile shows stiffness to the change in the heating strength at fixed density profile.

The initial plasma profile has radially increasing R/L_T. Initial turbulence front propagates radially inward, then the turbulence and temperature profile self-organizes with each other. During the self-organization of the temperature and turbulence, turbulent heat flux shows a self-regulated quasi-periodic bursty behavior, during which the turbulence intensity pulses. The self-organizing bursty structure shows ballistic convection radially outward. A clear correlation between the heat burst and opening up of the E × B shearing layer has been observed. As the eventual self-organized state settles in, the strong large scale bursty behavior disappears and the heat flux becomes of the 1/f avalanche type. Interaction of ITG turbulence with mean plasma is observed to be not only through η_i evolution, but also through the mean E × B (and possibly toroidal) flow.

For a more complete verification of the full-f XGC1, at least, a comparison with other full-f codes is needed. Such work is in progress and a manuscript on comparison with the full-f code GYSELA is in preparation (with G. Dif-Pladalier).

We note here that the simulation presented here is electrostatic without particle transport, with fixed magnetic equilibrium, and without turbulence interaction with plasma current. Addition of kinetic electrons and electromagnetic effect[46], including tearing modes, to XGC1 turbulence study is the nearest term improvement goal. More experimentally relevant physics effects are to be included later. A routine to evolve magnetic equilibrium and q profile along with the background plasma profile evolution is already incorporated in the sister code and will be used in XGC1. Other routines readily available from XGC0 include toroidal torque source and Monte Carlo neutral transport and recycling. Analytic model magnetic ripple capability is already incorporated into XGC1.

Acknowledgments

[1] R. Aymar, V.A. Chuyanov, M. Huguet, Y. Shimomura, ITER Joint Central Team, and ITER Home Teams. *Nucl. Fusion*, 41:1301, 2001.

[2] Y. Idomura, H. Urano, N. Aiba, and S. Tokuda. *Nucl. Fusion*, 49:065029, 2009.

[3] X. Garbet, Y. Sarazin, V. Grandgirard, G. Dif-Pradalier, G. Darmet, Ph. Ghendrih, P. Angelino, P. Bertrand, N. Besse, E. Gravier, P. Morel, E. Sonnendrucker, N. Crouseilles, J.-M. Dischler, G. Latu, E. Violard, M. Brunetti, S. Brunner, X. Lapillonne, T.-M. Tran, L. Villard, and M. Boulet. *Nucl. Fusion*, 47:1206, 2007.

[4] J. A. Heikkinen, S. Henriksson, S. Janhunen, T. P. Kiviniemi, and F. Ogando. *Contrib. Plasma Phys.*, 46:490, 2006.

[5] H. Biglari, P.H. Diamond, and M.N. Rosenbluth. *Phys. Fluids B*, 1:109, 1989.

[6] W. Horton. *Rev. Mod. Phys*, 71:735, 1999.

[7] C. S. Chang and S. Ku. *Phys. Plasmas*, 15:062510, 2008.

[8] C. S. Chang, S. Ku, P. Diamond, Z. Lin, S.Parker, T.S. Hahm, and N. Samatova. *Phys. Plasmas*, 16:056108, 2009.

[9] W. X. Wang, N. Nakajima, M. Okamoto, and S. Murakami. *Plasma Phys. Controlled Fusion*, 41, 1999.

[10] X. Q. Xu and M. N. Rosenbluth. *Phys. Fluids B*, 3, 1991.

[11] A. M. Dimits and B. I. Cohen. *Phys. Rev. E*, 49, 1994.

[12] Z. Lin, W. M. Tang, and W. W. Lee. *Phys. Plasmas*, 2, 1995.

[13] C. S. Chang and S. Ku. *Phys. Plasmas*, 11:2649, 2004.

[14] C. S. Chang and S. Ku. *Contrib. Plasma Phys.*, 46:496, 2006.

[15] W.M. Manheimer, M. Lampe, and G Joyce. *J. Comp. Phys.*, 138, 1977.

[16] B. A. Carreras, D. Newman, V. E. Lynch, and P.H. Diamond. *Phys. Plasmas*, 3, 1996.

[17] P.H. Diamond and T.S. Hahm. *Phys. Plasmas*, 2, 1995.

[18] X. Garbet, Y. Sarazin, P. Beyer, P. Ghendrih, R.E. Waltz, M. Ottaviani, and S. Benkadda. *Nucl. Fusion*, 2, 1995.

[19] A. M. Dimits, G. Bateman, M. A. Beer, B. I. Cohen, W. Dorland, G. W. Hammett, C. Kim, J. E. Kinsey, M. Kotschenreuther, A. H. Kritz, L. L. Lao, J. Mandrekas, W. M. Nevins, S. E. Parker, A. J. Redd, D. E. Shumaker, R. Sydora, and J. Weiland. *Phys. Plasmas*, 7:969, 2000.

[20] L. L. Lao, H. St. John, R. D. Stambaugh, A.G. Kellman, and W. Pheiffer. *Nucl. Fusion*, 25:1611, 1985.

[21] R. White. *Phys. Fluid B*, 2:845, 1990.

[22] A.H. Boozer. *Phys. Fluids*, 27:2441, 1984.

[23] R.G. Littlejohn. *Phys. Fluids*, 28:2015, 1985.

[24] Y. Nishimura, Z. Lin, J.L.V. Lewandowski, and S. Ethier. *J. Comp. Phys.*, 214:657, 2006.

[25] A. Bottino, A. G. Peeters, O. Sauter, J. Vaclavik, L. Villard, and ASDEX Upgrade Team. *Phys. Plasmas*, 11, 2004.

[26] Yasuhiro Idomura, Shinji Tokuda, and Yasuaki Kishimoto. *J. Plasma Fusion Res. SERIES*, 6, 2004.

[27] W. W. Lee. *Phys. Fluids*, 26:556, 1983.

[28] J.L. Luxon. *Nucl. Fusion*, 42:614, 2002.

[29] F. L. Hinton and R. D. Hazeltine. *Rev. Mod. Phys.*, 48:239, 1976.

[30] C.S. Chang and F.L. Hinton. *Phys. Fluids*, 25:1493, 1982.

[31] C.S. Chang and F.L. Hinton. *Phys. Fluids*, 29:3314, 1986.

[32] X. Q. Xu, E. Belli, K. Bodi, J. Candy, C. S. Chang, B. I. Cohen, R. H. Cohen, P. Colella,

A. M. Dimits, M. R. Dorr, Z. Gao, J. A. Hittinger, S. Ko, S. Krasheninnikov, G. R. McKee, W. M. Nevins, T. D. Rognlien, P. B. Snyder, J. Suh, and M. V. Umansky. *Nucl. Fusion*, 49:065023, 2009.

[33] H. Sugama and T.-H. Watanabe. *J. Plasma Phys*, 72:825, 2006.

[34] F. L. Hinton and M. N. Rosenbluth. *Plasma Phys. Control. Fusion*, 41:A653, 1999.

[35] G. Rewoldt, W. M. Tang, and M. S. Chance. *Phys. Fluids*, 25:480, 1982.

[36] G. Rewoldt, W. M. Tang, and R. J. Hastie. *Phys. Fluids*, 30:807, 1987.

[37] Z. Lin and T.S. Hahm. *Phys. Plasmas*, 11:1099, 2004.

[38] Z. Lin, T. S. Hahm, W. W. Lee, W. M. Tang, and R. B. White. *Science*, 281:1835, 1998.

[39] Y. Idomura, S. Tokuda, and Y. Kishimoto. *Nucl. Fusion*, 43:234, 2003.

[40] G. Dif-Pradalier, V. Grandgirard, Y. Sarazin, X. Garbet, Ph. Ghendrih, and P. Angelino. *Phys. Plasma*, 15:042314, 2008.

[41] T.S. Hahm, P.H. Diamond, and Z. Lin. *Phys. Plasmas*, 12:090903, 2005.

[42] D. Gurcan, P. H. Diamond, and T. S. Hahm. *Phys. Plasmas*, 14:055902, 2007.

[43] X. Garbet, Y. Sarazin, F. Imbeaux, P. Ghendrih, O. D. Gurcan C. Bourdelle, and P. H. Diamond. *Phys. Plasmas*, 14:122305, 2007.

[44] P. Beyer, S. Benkadda, G. Fuhr-Chaudier, X. Garbet, Ph. Ghendrih, and Y. Sarazin. *Phys. Rev. Lett.*, 94:105001, 2005.

[45] P. Diamond, S-I Itoh, K. Itoh, and T.S. Hahm. *Plasma Phys. Control. Fusion*, R35, 2005.

[46] J. Candy and R.E. Waltz. *Phys. Rev. Lett.*, 91, 2003.

Figure Captions

Figure 1. Relative change in canonical angular momentum P_ϕ from the error in the 3rd order predictor-corrector solution of the Lagrangian equation of motion is on the order 10^{-8} over a significant fraction of a typical turbulence simulation period.

Figure 2. Rapid approaches of the XGC1 solution to the exact cylindrical solution as the inverse aspect ratio is reduced. At $\epsilon = r/R_0 = 0.0895$ the red (XGC1 solution) and black (exact cylindric analytic) curves are already visually indistinguishable.

Figure 3. Verification of the neoclassical poloidal rotation in full-f XGC1 in a realistic DIII-D geometry (g096333.03337). (a) The solid line is the radial electric field E_r obtained when we use the collisionality-dependent analytic formula of Hinton-Hazeltine [29] on the radial plasma profiles from XGC1 and the dashed line with X-mark is what is actually obtained in XGC1. Corrugation on the analytic result is from differentiation of the numerical profile data. (b) Radial profile of particle density and (c) radial profile of initial and final ion parallel temperature from the code. The q-profile is given in Figure 11(b).

Figure 4. (a) Ion thermal conductivity from XGC1 is compared with the Chang-Hinton formula [30, 31]. (b) Initial and final parallel temperature profile and (c) radial electric field from the simulation are shown together. Concentric circular flux surface is used for this study with q=2 and a flat density $5 \times 10^{19} m^{-3}$. The radial electric field quickly establishes an ion orbit time and stay steady during the temperature relaxation.

Figure 5. Damping rate γ_0 of GAM versus the safety factor q in comparison with a known analytic theory in delta-f mode (quoted from Ref. [32]), demonstrating a satisfactory result from XGC1 (red diamond).

Figure 6. Collisionless residual potential from GAM oscillation in XGC1 agrees well with the analytic result of Hinton and Rosenbluth [34]. Safety factor q=1.5 is used in this study and $\tau_{bi} = 2\pi R/\sqrt{2}v$, where $v = (kT_i/m_i)^{1/2}$.

Figure 7. The linear ITG growth rate and the real frequency from (a) XGC1 in delta-f cyclone plasma is compared against the result from (b) the linear eigenvalue code FULL[35, 36] and a gyrokinetic particle code GTC [37] in the global cyclone geometry with $R/L_T = 6.9$. The results shown here compare equally well with other benchmarking studies reported in Ref. [19].

Figure 8. Comparison of the delta-f ion thermal conductivity χ_i behavior in time, between XGC1 in delta-f mode and the core gyrokinetic particle code GTC in the global cyclone

geometry.

Figure 9 Comparison of XGC1 between the delta-f and full-f modes.(a) Heat conductivity change in time, (b) R/L_T change in time, and (c) Heat conductivity vs. R/L_T are plotted. Both the heat conductivity and the R/L_T show reasonable convergence to each other.

Figure 10. Initial plasma density and temperature profiles. Electron temperature is assumed to be equal to ion temperature. Gradient scale lengths relative to the major radius on magnetic axis are shown together.

Figure 11. (a) Relationship between the normalized poloidal flux ψ_N and real distance in meters from the magnetic axis (at R_{axis}) to the flux surface (at R) along the midplane. (b) Radial profile of the safety factor q.

Figure 12. (a) Representative χ_i results from convergence tests in marker particle numbers (average 800, 1,600, 3,200, and 12,800 particles per node). It appears to be that 800 particles per node might be good enough. However, (b) test of R/L_T shows that at least 1,600 particles per node is needed.

Figure 13. Time behavior of the effective ion thermal conductivity and the turbulence amplitude squared in MKS unit across the $\psi_N = 0.45$ surface.

Figure 14. The neoclassical ion thermal conductivity of the system (solid) and the total turbulent-neoclassical ion thermal conductivity (dashed) at the relatively steady final stage.

Figure 15. Two dimensional electric potential contour for $\Phi - \Phi_{0,0}$ on a constant toroidal angle plane in the middle of the bursty nonlinear relaxation stage.

Figure 16. 2D contour plot of (a) E × B shearing rate strength, (b) bursty heat fluxes and (c) E × B shearing rate in the beginning of the steady turbulence stage.

Figure 17. Out-of-phase time behavior between the heat flux and the E × B shearing strength at $\psi_N = 0.45$.

Figure 18. Temperature gradient behavior in time at three adjacent radial locations.

Figure 19. Frequency spectrum of the heat flux in the middle of the simulation radii ($\psi_N = 0.3$) in the bursty stage and in the final quasi-steady state.

Figure 20. (a) R/L_T profiles are drawn at the initial, after the initial settling down before turbulence, and in the self-organized stage near the end of the simulation. (b) Comparison between the initial and final ion temperature profiles. The self-organized ion temperature profile becomes stiff in variation of heat source strength.

Figure 21. Growth of linear ITG mode for different values of ion temperature gradient

R/L_T in the DIII-D geometry. ITG approaches marginal stability at $R/L_T = 4$ and ITG at $R/L_T \sim 6.5$ is strongly unstable linearly.

Figure 22. $E_r \times B$ poloidal rotation speed profile in ψ_N at three different times: after the large amplitude GAM jittering before the turbulence generation $(60R/v_i)$, in the middle of the bursty turbulence phase $(180R/v_i)$, and during the avalanche phase $(400R/v_i)$.

Figure 23. Radial correlation length of (a) $E_{r(0,0)}$ and (b) δE_r turbulence activities during the bursty (100-300 R/v_i) and steady (400-600 R/v_i) turbulence transport activities.

Figure 24. Energy accounting within $0.3 \leq \psi_N \leq 0.7$ between the total influx across the inner boundary (black curve) and the sum of the consumed energy (blue curve) to the particles, the electric field, and across the outer boundary. Red line shows sum of black and blue curves. About 2% error is noticed. Unlike in a delta-f particle code, error in a full-f code does not grow in principle since the particle weights do not grow.